

Wall loss of atomic nitrogen determined by ionization threshold mass spectrometry

M. Sode, T. Schwarz-Selinger, W. Jacob, and H. Kersten

Citation: [Journal of Applied Physics](#) **116**, 193302 (2014); doi: 10.1063/1.4902063

View online: <http://dx.doi.org/10.1063/1.4902063>

View Table of Contents: <http://scitation.aip.org/content/aip/journal/jap/116/19?ver=pdfcov>

Published by the [AIP Publishing](#)

Articles you may be interested in

[Electrical characterization of the flowing afterglow of N₂ and N₂/O₂ microwave plasmas at reduced pressure](#)

[J. Appl. Phys.](#) **115**, 163303 (2014); 10.1063/1.4872468

[Temperature and density evolution during decay in a 2.45 GHz hydrogen electron cyclotron resonance plasma: Off-resonant and resonant cases](#)

[Rev. Sci. Instrum.](#) **84**, 093301 (2013); 10.1063/1.4819875

[Time-resolved measurements of the E -to- H mode transition in electronegative pulse-modulated inductively coupled plasmas](#)

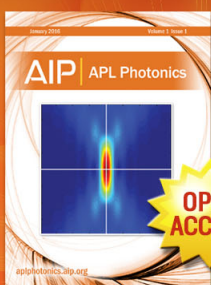
[J. Vac. Sci. Technol. A](#) **24**, 2151 (2006); 10.1116/1.2359736

[Measurement and modeling of molecular ion concentrations in a hydrogen reflex-arc discharge](#)

[Phys. Plasmas](#) **9**, 4330 (2002); 10.1063/1.1503070

[Determination of negative ion density with optical emission spectroscopy in oxygen afterglow plasmas](#)

[Appl. Phys. Lett.](#) **72**, 2391 (1998); 10.1063/1.121394



Launching in 2016!
The future of applied photonics research is here

AIP | APL
Photonics

Wall loss of atomic nitrogen determined by ionization threshold mass spectrometry

M. Sode,^{1,a)} T. Schwarz-Selinger,¹ W. Jacob,¹ and H. Kersten²

¹Max-Planck-Institut für Plasmaphysik, Boltzmannstraße 2, D-85748 Garching, Germany

²Institute for Experimental and Applied Physics, Christian-Albrechts-Universität zu Kiel, Leibnizstraße 11-19, D-24098 Kiel, Germany

(Received 2 October 2014; accepted 7 November 2014; published online 19 November 2014)

In the afterglow of an inductively coupled N₂ plasma, relative N atom densities are measured by ionization threshold mass spectrometry as a function of time in order to determine the wall loss time t_{wN} from the exponential decay curves. The procedure is performed with two mass spectrometers on different positions in the plasma chamber. t_{wN} is determined for various pressures, i.e., for 3.0, 5.0, 7.5, and 10 Pa. For this conditions also the internal plasma parameters electron density n_e and electron temperature T_e are determined with the Langmuir probe and the rotational temperature $T_{rot}^{N_2}$ of N₂ is determined with the optical emission spectroscopy. For $T_{rot}^{N_2}$, a procedure is presented to evaluate the spectrum of the transition $v' = 0 \rightarrow v'' = 2$ of the second positive system ($C^3\Pi_u \rightarrow B^3\Pi_g$) of N₂. With this method, a gas temperature of 610 K is determined. For both mass spectrometers, an increase of the wall loss times of atomic nitrogen with increasing pressure is observed. The wall loss time measured with the first mass spectrometer in the radial center of the cylindrical plasma vessel increases linearly from 0.31 ms for 3 Pa to 0.82 ms for 10 Pa. The wall loss time measured with the second mass spectrometer (further away from the discharge) is about 4 times higher. A model is applied to describe the measured t_{wN} . The main loss mechanism of atomic nitrogen for the considered pressure is diffusion to the wall. The surface loss probability β_N of atomic nitrogen on stainless steel was derived from t_{wN} and is found to be 1 for the present conditions. The difference in wall loss times measured with the mass spectrometers on different positions in the plasma chamber is attributed to the different diffusion lengths. [<http://dx.doi.org/10.1063/1.4902063>]

I. INTRODUCTION

Plasma process technology plays an important role in a wide range of different industrial applications such as semiconductors, solar cells, and display manufacturing. Reactive plasmas are used for etching, coating, and surface treatment. In a large variety of cases, etching or deposition processes are based on the reactivity of the radical particles involved. Therefore, quantifying the radical particle densities is a first and important step for an improved understanding of plasma-surface-interaction processes. One relevant radical is atomic nitrogen, used in semiconductor manufacturing for nitridation, for example, in the fabrication of gate insulators or interlayer dielectric films.^{1,2} For low-pressure plasmas, atomic nitrogen is mainly produced by electron-induced dissociation of N₂ which is predominantly affected by the electron density and electron temperature of the respective plasma. The loss of atomic nitrogen in such plasmas is determined by the flux to the wall.^{3–8} In our case, as in most other cases, the wall loss is determined by recombination of atomic nitrogen to form molecular nitrogen which desorbs from the surface. This wall loss of atomic nitrogen is described by the surface loss probability β_N which is a material specific property. Kersten *et al.*⁹ studied the energy flux with a thermal probe in the spacial afterglow of a N₂ plasma. They changed the substrate material of the thermal probe

under comparable experimental plasma conditions so that the N influx was the same for all studied substrate materials. They observed that the power influx of the recombining radicals onto the surface of the thermal probe depends sensitively on the material substrate of the thermal probe. This was interpreted by different β_N values for the different materials.

β_N is not only different for different materials, but even for the same material published values for β_N vary between different experiments. Since the recombination process of radicals on surfaces and, hence, β_N are a function of the surface temperature, a possible explanation for different β_N could be the different surface temperatures. Furthermore, it has to be kept in mind that β_N values are in general determined from measured data on the basis of a diffusion model which describes the transport of the radical particles to the chamber walls. This evaluation procedure depends to a large extent on assumptions on the relevant geometry of the plasma chamber and on the assumption about the N atom temperature. In principle, there are several methods to obtain experimental values of β_N . The first method is to measure the power influx onto a thermal probe in the spacial afterglow as mentioned above (see, e.g., Refs. 9–11). However, for this method, the absolute density and temperature of atomic nitrogen n_N has to be known. Another method is to apply a rate equation model with further input parameters, i.e., electron density and electron temperature to derive β_N indirectly from the atomic N density in the steady state

^{a)}Electronic mail: maik.sode@ipp.mpg.de

plasma, as applied by Singh *et al.*⁴ However, this indirect method is charged with a larger uncertainty due to error propagation of the uncertainties of the various input parameters. The third method is to measure the decay of the N atom density in the temporal afterglow of a N₂ plasma. With this method, t_{wN} is measured directly. There exist several spectroscopic methods for detecting the radical density time-resolved with a high time resolution of the order of milliseconds or even microseconds: vacuum ultra violet absorption spectroscopy (VUVAS),⁵ two-photon-absorption laser-induced fluorescence (TALIF),^{6,7} and quantum cascade laser absorption spectroscopy (QCLAS).¹²

In the work presented here, relative N atom densities were measured in the afterglow of pure N₂ plasmas as a function of time by ionization threshold mass spectrometry (ITMS) in order to determine the wall loss time t_{wN} . The wall loss times were determined for various pressures and from these data the surface loss probability of atomic nitrogen on stainless steel β_N was derived. The procedure is performed with two independent mass spectrometers at different positions in the plasma chamber. The first mass spectrometer (plasma monitor, PM) is located in the radial center of the plasma chamber measuring the atomic nitrogen density of the hot plasma zone. The second mass spectrometer (molecular-beam mass spectrometer, MBMS) measures the radical density on the radial side walls of the plasma chamber far away from the hot plasma zone. To our knowledge, measurements of the wall loss time at two different positions in the same plasma chamber were not yet published neither for nitrogen nor for other wall loss times of radical species such as hydrogen or oxygen. In addition, contrary to most spectroscopic determination⁵⁻⁷ of the nitrogen radical density where the density is averaged over the line of sight, this work measures the local radical density at two very different positions.

II. EXPERIMENT

A. Experimental setup

The experimental setup consists of a cylindrical stainless steel plasma chamber shown schematically in Fig. 1. A detailed description of the experimental set-up can be found in Ref. 13. In short, the discharge is generated by inductive coupling using a planar coil with 5 turns and 100 mm in diameter. The coil is driven by a radio frequency (rf) generator operating at 13.56 MHz with a maximum power of 600 W (Dressler Cesar 136). The coil is separated from the vacuum chamber by a quartz dome.¹⁴ The top part of the dome is 10 mm thick and acts as the dielectric window for the rf power. The outer diameter d_{el} of the quartz dome and the stainless steel electrode which is located opposite the dielectric window is $d_{el} = 2r_{el} = 131$ mm, where r_{el} is the corresponding radius. The axial distance l_{el} between the electrode and the quartz window is 60 mm. At r_{el} , there is no radial side wall between the electrode and dielectric window. The stainless steel vacuum chamber has a radius of $r_{ch} = 125$ mm and a total height of $l_{ch} = 360$ mm. For the description of the plasma chamber setup, a coordinate system with cylindrical geometry (r —radial component, l —axial component) is used

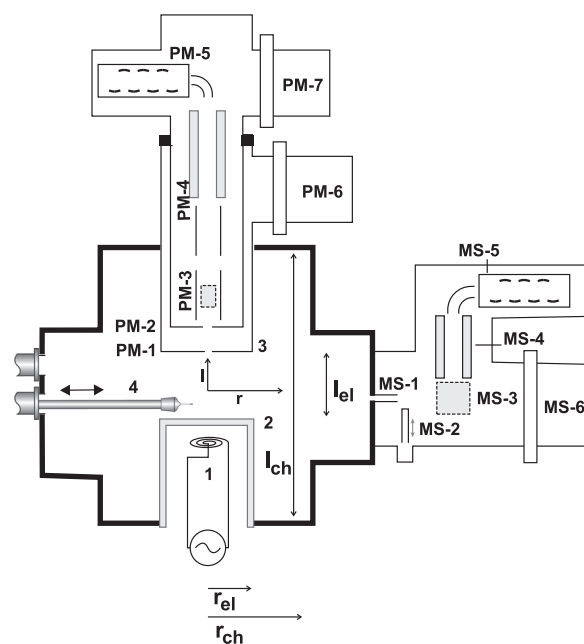


FIG. 1. Schematic representation of the plasma chamber: 1—planar inductive coil, 2—quartz dome, 3—stainless steel housing for the PM, 4—Langmuir probe. Plasma monitor set-up: PM-1—first orifice (100 μ m), PM-2—second orifice (500 μ m), PM-3—ion optics and ionizer, PM-4—energy and mass analyzer, PM-5—secondary electron multiplier, PM-6—first pumping stage, PM-7—second pumping stage. Molecular-beam mass spectrometer set-up: MS-1—capillary tube, MS-2—shutter, MS-3—cross-beam ion source, MS-4—quadrupole mass filter, MS-5—secondary electron multiplier, MS-6—pumping system.

whose origin is placed at the radial center of the plasma chamber 30 mm below the stainless steel electrode (see also Fig. 1).

The plasma chamber is pumped by a turbo molecular pump with Hohlweck stage. The incoming gas flows are adjusted with mass-flow controllers. The working pressure is measured with a capacitance manometer before plasma ignition. The pressure stays constant within the experimental uncertainty of 2% of the capacitance manometer when the plasma is ignited.

The electron energy distribution function (EEDF), the electron temperature T_e , and the electron density n_e were determined by a single-tip Langmuir probe system.¹³ T_e is calculated by the potential difference $\Delta V = V_{pl} - V_{fl}$ method,¹³ where V_{pl} and V_{fl} denote the plasma and the floating potential, respectively, and n_e is calculated by integrating the EEDF.¹³ The Langmuir probe measurements were performed in the center of the plasma ($r = 0$ mm), 20 mm above the quartz window.

Optical emission spectroscopy (OES) was applied to measure the gas temperature. The used spectrometer was a Czerny-Turner spectrograph (Acton SpectraPro 275) with a focal length of 275 mm. The experiments were conducted with a 1800 lines/mm grating, which has a measured resolution of 0.15 nm at $\lambda = 600$ nm. The light was detected by a CCD array (EEV 256 \times 1024 OE CCD30, PIXIS, Princeton Instruments). The measured signal $D(\lambda)$ (in arbitrary units) results from the emitted photons integrated along the line of sight through the plasma as a function of the wavelength λ in

a time interval t_{int} . The signal was relatively quantified by multiplying with the relative sensitivity curve $R(\lambda)$ obtained for our experimental setting using a calibrated halogen lamp and D₂ arc discharge light source for calibration.^{8,13}

For radicals, the density in the afterglow and hence the signal intensity is low. To increase counting statistics, repetition of the afterglow state is necessary. To obtain a high repetition rate of the afterglow, a pulsed plasma was used. The pulsed plasma is operated with a power-on phase (P_{on}) with a duration of t_{on} and a power-off phase (P_{off}) with a duration of t_{off} . $P_{on} + P_{off}$ are repeated with the cycle number m_{cycle} . A pulse generator is used which switches on and off the rf generator and provides the trigger signal for the mass spectrometer measurements. The signal pulses (measuring events) of the secondary electron multipliers (SEMs) of our two mass spectrometers are detected by multi-channel scaler cards (MCS, 65536 channels, Ortec). The MCS card sorts these events according to time into a selected number of channels of width t_{dwell} from the beginning of the trigger signal. The statistical error of the counting events N is \sqrt{N} . The signal S is computed from $S = N/\Delta t$ with $\Delta t = m_{cycle} \times t_{dwell}$ and has the unit counts per second (cps). In the same manner, the error of S is obtained ($\Delta S = \sqrt{N}/\Delta t$). The time resolution t_{dwell} per channel applied in the measurements was chosen between 0.1 ms and 0.4 ms.

B. Mass spectrometer setups

The plasma is mainly generated in the assumed cylinder with the volume $V = \pi r_{el}^2 l_{el}$ between the stainless steel electrode and the quartz window.¹⁵ An energy-resolving mass spectrometer¹³ (PM) is used to measure the relative radical density in the plasma volume. The PM is incorporated into the upper, grounded electrode in the radial center of the plasma chamber. In addition, a MBMS is used to measure the radical density on the radial side walls of the plasma chamber. The MBMS is located about 200 mm from the discharge center in the central plane (at $l = 0$ mm). A detailed description of the PM and the MBMS can be found in Refs. 13, 16, 17, and 18, respectively.

The PM is twofold differentially pumped resulting in a background pressure in the plasma monitor vacuum section of the order of 10^{-6} Pa for a working pressure of 1 Pa in the plasma chamber. Particles are sampled through two aligned orifices 100 and 500 μ m in diameter, respectively, and are detected by a SEM. The PM is here used in the mode for measuring neutrals only. The entrance lens of the PM is set to a voltage of +100 V so that plasma ions cannot reach the detector.

The MBMS samples particles at the side wall of the plasma chamber through a carbon tube with an inner diameter of 600 μ m and a length of 12 mm. The background pressure in the mass spectrometer chamber is of the order of 10^{-6} Pa for a working pressure of 1 Pa in the plasma chamber. In addition, the mass spectrometer chamber is equipped with a stainless steel shutter behind the orifice to allow distinguishing the isotropic background signal coming from the background pressure from the signal due to the molecular beam that is formed by the tube. The particle density in this

molecular beam is proportional to the particle density in the vessel.¹⁹ The beam-to-background ratio R is mass-dependent and yields for N₂ $R_{N_2} = 4.4 \pm 0.3$ and for H₂ $R_{H_2} = 1.5 \pm 0.1$. When the MBMS is used to measure atomic nitrogen (see Sec. IV), no significant signal is detected if the stainless steel shutter blocks the radical beam. That means, the signal of atomic nitrogen has no measurable background but consists only of the collimated beam.

III. ROTATIONAL TEMPERATURE OF N₂

A. Calculation of the spectrum of N₂ (V_{02}^{SPS})

For modeling the wall loss, it is important to have knowledge of the gas temperature. Therefore, a method for determining the gas temperature in low-temperature nitrogen plasmas will be presented in the following. A frequently used method is the measurement of the rotational temperature of the excited state $C^3\Pi_u$ of the N₂ molecule.^{20–25} In the following, the correlation between $T_{rot}^{N_2}$ and T_g as well as the determination of $T_{rot}^{N_2}$ from the line intensity of the rotational spectrum will be presented. The translational energy of N₂ molecules is determined by collisions with gas molecules as well as with the plasma-surrounding wall. A fast thermalization between translation and rotation occurs due to collisions so that $T_{rot}^{N_2} \approx T_g$.^{22–24,26} By electron impact excitation of the ground state, the rotational population distribution is directly transferred to the excited state since the electron is too light to change the rotational momentum. A more detailed discussion of the conditions of this method can be found in Biloiu *et al.*²⁶ In the present work, the electronic transition of $C^3\Pi_u \rightarrow B^3\Pi_g$ of the N₂ spectrum of the second positive system (SPS) is considered. From this, the established vibrational transition $v' = 0 \rightarrow v'' = 2$ is used,^{22,23} which is hereafter abbreviated with V_{02}^{SPS} . The line intensity $\dot{N}_{p'v'J',p''v''J''}^{p'v'J'}$ in the unit of photons per volume and time is the product of the transition probability $A_{p'v'J',p''v''J''}^{p'v'J'}$ from state $p'v'J'$ into state $p''v''J''$ and the population density $n_{p'v'J'}$ of the state $p'v'J'$. In a vibrational transition of an electronic transition, the line intensities $\dot{N}_{J''}^{J'}$ of the rotational bands of the considered transition are a function of the following variables:^{23,25,27}

$$\dot{N}_{p'v'J',p''v''J''}^{p'v'J'} \propto \left(\lambda_{p'v'J',p''v''J''}^{p'v'J'} \right)^{-3} \times S_{J''}^{J'} \times \exp \left(- \frac{E_{rot}^{J'}}{k_B T_{rot}^{v'}(C^3\Pi_u)} \right) \equiv \dot{N}_{J''}^{J'} \quad (1)$$

($\lambda_{p'v'J',p''v''J''}^{p'v'J'}$ —wavelength of the transition, $E_{rot}^{J'}$ —rotational energy, $T_{rot}^{v'}$ —rotational temperature, $S_{J''}^{J'}$ —Hönl-London factor). The rotational energy is expressed as follows:

$$E_{rot}^{J'} = B_v J'(J' + 1) - D_e J'^2 (J' + 1)^2, \quad (2)$$

and

$$B_v = B_e - \alpha(v + 1/2). \quad (3)$$

B_e , α , and D_e are molecular constants for the different electronic states. Their used values are given in Table I.

For the considered transition, the coupling of rotation and electronic motion is according to Hund's case (a).²⁹ The

TABLE I. Used molecular constants of N₂ for various electronic states p (taken from Ref. 28).

p	$B_e(\text{cm}^{-1})$	$\alpha(\text{cm}^{-1})$	$D_e(\text{cm}^{-1})$
$X^1\Sigma_g^+$	1.998	0.0173	0.00000573
$B^3\Pi_g$	1.63772	0.01816	0.00000584
$C^3\Pi_u$	1.82677	0.024	0.00000511

Hönl-London factors are taken from Ref. 25 and are expressed for the P ($\Delta J = J' - J'' = -1$), Q ($\Delta J = 0$), and R ($\Delta J = 1$) branch as follows:

$$S_{J''=J'+1}^{J'} = 6(J' + 1) - 10/(J' + 1) \quad (4)$$

$$S_{J''=J'}^{J'} = 10/J' + 10/(J' + 1) \quad (5)$$

$$S_{J''=J'-1}^{J'} = 6J' - 10/J'. \quad (6)$$

In Eq. (1), it can be seen that with the exception of molecular constants, the only variable of $\dot{N}_{J''}^{N_2}$ is $T_{rot}^{N_2}$. Therefore, a spectrum can be calculated and fitted to the measured spectrum by the variation of $T_{rot}^{N_2}$.

In practise, line broadening caused by the optical spectrometer adds another fitting parameter. In the following, a method is described based on Biloiu *et al.*²⁶ which takes this line broadening into account. For the mathematical description of this line broadening a Gaussian function is used

$$f(w, \lambda_x, \lambda_{0,J''}) = \frac{\sqrt{4\ln 2}}{\sqrt{\pi}w} \exp\left[-\frac{4\ln 2}{w^2}(\lambda_x - \lambda_{0,J''})^2\right], \quad (7)$$

where λ_x is the spectrometer wavelength which is set by the measuring channels of the CCD array. $\lambda_{0,J''}$ denotes the theoretical wavelength position of the observed rotational line, respectively. w is the line width (full width at half maximum—FWHM). The intensities of the P, Q, and R branch for the quantum numbers $J' = 0 - 70$ are calculated. To compare the calculated intensities \dot{N}_x^c with the measured intensities \dot{N}_x^m , all the contributions of the individual intensities at a wavelength λ_x have to be considered

$$\dot{N}_x^c(\lambda_x) = \sum_{P,Q,R} \sum_{J=1'}^{70} f(w, \lambda_x, \lambda_{0,J''}) \times \dot{N}_{J''}^{J'}(\lambda_{0,J''}, T_{rot}^{N_2}). \quad (8)$$

The calculated and measured spectra are normalized to the respective maximum intensity \dot{N}_{max} . In the experimental spectrum, the wavelength scale is shifted such that the maxima of the calculated and the measured spectrum match. The spectra normalized to their respective maxima are compared and χ^2 is calculated

$$\chi^2(T_{rot}^{N_2}, w) = \sum_{x=1}^Z \left[\frac{\dot{N}_x^m / \dot{N}_{max}^m - \dot{N}_x^c / \dot{N}_{max}^c(T_{rot}^{N_2}, w)}{\Delta(\dot{N}_x^m / \dot{N}_{max}^m)} \right]^2 \quad (9)$$

($\dot{N}_x^m / \dot{N}_{max}^m$ —relative line intensity of the measured spectrum, $\Delta(\dot{N}_x^m / \dot{N}_{max}^m)$ —corresponding error of the measured spectrum, $(\Delta(\dot{N}_x^m / \dot{N}_{max}^m)) / (\dot{N}_x^m / \dot{N}_{max}^m) = 5\%$, which was estimated by repeating the measurement series once),

$\dot{N}_x^c / \dot{N}_{max}^c$ —relative line intensity of the calculated spectrum, x —index of selected wavelength in the spectrometer, Z —number of considered wavelength channels of the measured spectrum). The rotational temperature of the measured spectrum is determined by minimizing χ^2 through variation of $T_{rot}^{N_2}$ and w in Eq. (9). For the vibrational transition $v' = 0 \rightarrow v'' = 2$, the wavelength range between 377.24 nm and 380.75 nm with $Z = 78$ is considered. For the calculation of the spectrum, the rotational temperature in the excited state $T_{rot}^{v'}(C^3\Pi_u)$ is important (see also Eq. (1)). However, for the processes in the plasma, the rotational temperature in the ground state is decisive. The rotational population distribution of the ground state is related to the rotational population distribution of the excited state as:

$$T_{rot}^{v=0}(X^1\Sigma_g^+) = \frac{B_{v=0}(X^1\Sigma_g^+)}{B_{v'=0}(C^3\Pi_u)} T_{rot}^{v'=0}(C^3\Pi_u). \quad (10)$$

Here, $B_{v=0}(X^1\Sigma_g^+)$ and $B_{v'=0}(C^3\Pi_u)$ denote the rotational constants of the lowest vibrational state of the ground state and from V_{02}^{SPS} , respectively. In the present work, a $B_{v=0}(X^1\Sigma_g^+) / B_{v'=0}(C^3\Pi_u)$ of 1.10 is used which is calculated from data of Ref. 28. In the following, $T_{rot}^{N_2}$ is always given for the ground state of N₂.

The error of the rotational temperature $\Delta T_{rot}^{N_2}$ is 30 K (see Refs. 20 and 22).

B. Comparison with a measured spectrum of N₂ (V_{02}^{SPS})

In Fig. 2, a measured spectrum for V_{02}^{SPS} of N₂ is shown together with the corresponding calculated spectrum. The measurement was performed in a H₂-N₂-Ar-Plasma at $f_{N_2} = 56\%$, $p = 1.5$ Pa, and $P = 200$ W. The spectrum consists of a peak with a maximum at $\lambda_x = 380.66$ nm, a kink at $\lambda_x = 380.4$ nm and a tail to lower wavelengths. The calculated spectrum has a minimal χ^2 (see Eq. (9)) for a $T_{rot}^{N_2}$ of 480 K and a w of 0.16 nm ($\chi_{min}^2 = 9.2 \times 10^{-7}$).

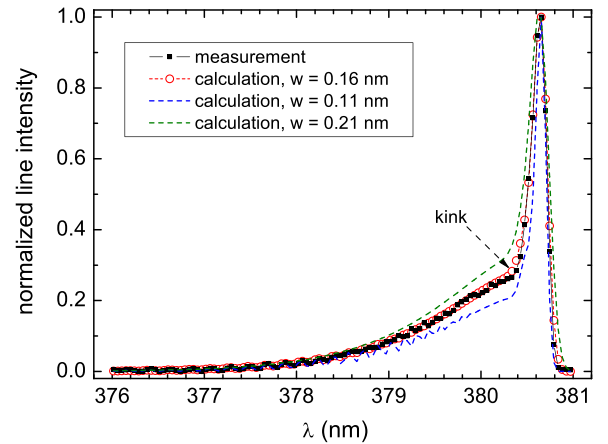


FIG. 2. Comparison between measured and calculated spectrum of the transition $v' = 0 \rightarrow v'' = 2$ of the second positive system ($C^3\Pi_u \rightarrow B^3\Pi_g$) of N₂. The plasma parameters are $p = 1.5$ Pa, $P = 200$ W, and $f_{N_2} = 56\%$. The parameters of the simulation where χ^2 is minimal are $w = 0.16$ nm and $T_{rot}^{N_2} = 480$ K. In addition, calculated spectra for line widths of $w = 0.11$ nm and $w = 0.21$ nm ($T_{rot}^{N_2} = 480$ K) are plotted.

A variation in $T_{rot}^{N_2}$ varies the height of the tail of the spectrum but leaves the width of the peak at $\lambda_x = 380.66$ nm unchanged. A variation in w varies the height and the shape of the tail as well as the width of the peak at $\lambda_x = 380.66$ nm. The wavelength range from about 379 to 380.4 nm is very well fitted for $w = 0.16$ nm. For larger or smaller values of w , the agreement between data and model is significantly worse. For comparison, model data for $w = 0.11$ and 0.21 nm are also shown in Fig. 2.

To cross-check if the line width $w = 0.16$ nm determined by the fit is appropriate, w was additionally determined by another method suggested by Biloiu *et al.*²⁶ in which the width of the atomic Ar I line at 415.86 nm is measured. Based on this method, a value for w of 0.11 ± 0.01 nm was determined in the present work. This value is significantly below the value of 0.16 nm obtained from χ^2 minimization. To confirm that $w = 0.16$ nm is the optimal value for the spectrometer resolution, the shape of the spectrum will be further discussed. For this purpose, spectra are calculated with a smaller and a larger value of w . These curves are presented as dashed lines in Fig. 2. For the first case with $w = 0.11$ nm, the tail (at $\lambda_x < 380.35$ nm) shows an oscillatory structure between $377.0 \lesssim \lambda_x \lesssim 379.5$ nm, i.e., at high J' . This oscillatory structure is not observed in the measured spectrum. The absence of the oscillatory structure suggests an actually lower resolution of the spectrometer than $w = 0.11$ nm. In the other extreme case for $w = 0.21$ nm in the range of $379.0 \lesssim \lambda_x \lesssim 380.5$ nm, the curve shape of the calculated spectrum deviates from the experimental spectrum. Summarizing, a difference in $w = 0.16$ nm of ± 0.05 nm leads to a significant deviation of the shape of the calculated spectrum and thus to a higher χ^2 . It is therefore concluded that $w = 0.16$ nm determined by χ^2 minimization is the correct parameter.

The spectrum of Fig. 2 was measured in a plasma with a gas mixture of H_2 and N_2 . The plasma parameters were $p = 1.5$ Pa, $P = 200$ W, and $f_{N_2} = 56\%$. Therefore, it is possible to compare $T_{rot}^{N_2}$ with the rotational temperature $T_{rot}^{H_2}$ of H_2 . The method for $T_{rot}^{H_2}$ was described in Ref. 13. $T_{rot}^{H_2}$ was derived from the rotational lines $Q_1 - Q_3$ of the Q-branch of the H_2 Fulcher- α diagonal band ($v' = v'' = 2$) with an experimental uncertainty of 50 K.¹³ For the plasma conditions of Fig. 2, a value of $T_{rot}^{H_2} = (490 \pm 50)$ K is derived which is within the experimental uncertainty identical with $T_{rot}^{N_2} = (480 \pm 30)$ K. In Ref. 21, agreement between $T_{rot}^{N_2}$ and $T_{rot}^{H_2}$ was observed, too.

IV. IONIZATION THRESHOLD MASS SPECTROMETRY

ITMS is used to measure the relative N atom density in the afterglow of N_2 plasmas as function of time to determine the wall loss time experimentally.

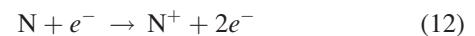
A. ITMS principle

In the ion source of a mass spectrometer, the incoming neutral particles are ionized by electron impact. The thus produced ions are separated according to their mass-to-charge ratio in the quadrupole and finally detected by the SEM. In general, the signal I of a mass spectrometer is

proportional to the energy-dependent cross section $\sigma(E_{e,iz})$ of the electron-collision reaction and the density n of the particles in the ionization chamber (see, e.g., Refs. 30 and 31)

$$I \propto \sigma(E_{e,iz}) \times n, \quad (11)$$

where $E_{e,iz}$ is the electron energy of the electrons in the ionizer (subscript “iz”). Typical ionization energies in the ionizer are 70 eV where the cross section is maximum for most species. At such electron energies, different electron-induced reactions are possible: direct ionization of a species, dissociative ionization of molecular species, or even multiple ionization. For example, when measuring N radicals which result from the parent molecule N_2 , two processes can contribute to the signal on the mass channel of N. On the one hand, the direct ionization:



on the other hand, the dissociative ionization:



Applying Eq. (11) to estimate the intensity ratio of N^+ originating from N ($I_{N \rightarrow N^+}$, Eq. (12)) to N^+ originating from N_2 ($I_{N_2 \rightarrow N^+}$, Eq. (13)) in a N_2 plasma gives the expression $I_{N \rightarrow N^+}/I_{N_2 \rightarrow N^+} = \sigma_{N \rightarrow N^+}/\sigma_{N_2 \rightarrow N^+} \times n_N/n_{N_2}$. For $E_{e,iz} = 70$ eV, $\sigma_{N \rightarrow N^+} = 1.3 \times 10^{-20} \text{ m}^2$ (Ref. 32) and $\sigma_{N_2 \rightarrow N^+} = 0.5 \times 10^{-20} \text{ m}^2$ (Ref. 33) are the cross section values for the direct ionization of atomic nitrogen and dissociative ionization of molecular nitrogen, respectively. For a typical dissociation degree of $n_N/n_{N_2} = 0.002$ (Ref. 16), this results in an intensity ratio of $I_{N \rightarrow N^+}/I_{N_2 \rightarrow N^+} \approx 0.005$ which means that for a N_2 plasma the mass spectrometer signal at $E_{e,iz} = 70$ eV on mass channel 14 amu/e nearly exclusively originates from the N_2 background gas and only 0.005 of the signal comes from direct ionization of N. Therefore, at 70 eV quantitative detection of radical particles from the plasma is practically impossible. ITMS exploits the fact that the energy threshold for reaction 13 is larger than that for reaction 12. The energies for other possible pathways are summarized in Table II. To suppress a signal contribution from the dissociative ionization, the electron energy $E_{e,iz}$ in the mass spectrometer has to be below the energy threshold of reaction 13. The signal intensity in the range of the threshold energies is small because the cross section of electron-induced ionization is very low.

TABLE II. Threshold energies E for ionization, excitation, and dissociation of atomic and molecular nitrogen.

Reaction	E (eV)	Source
$e^- + N \rightarrow N^+ + 2e^-$	14.5	34
$e^- + N \rightarrow N(D) + e^-$	2.4	35
$e^- + N \rightarrow N(P) + e^-$	3.6	35
$e^- + N_2 \rightarrow N^+ + N + 2e^-$	24.3	34
$e^- + N_2 \rightarrow N_2^+ + 2e^-$	15.6	36
$e^- + N_2 \rightarrow N_2(v = 10) + e^-$	2.7	36
$e^- + N_2 \rightarrow N_2(A) + e^-$	6.2	34
$e^- + N_2 \rightarrow 2N + e^-$	9.8	36

Because the extraction potential of the ion optics of a mass spectrometer in most cases penetrates into the ionizing volume of the ion source, the real electron energy in the extraction volume often differs from the set electron energy $E_{e,iz}$ which is determined by the applied ion source cathode voltage V_{cath} . This results in an ion-source-dependent shift of the ionization energy ($e \times \Delta V_{cath}$, see also Ref. 37). The electron energy $E_{e,iz}$ is then given by

$$E_{e,iz} = e \times (V_{cath} + \Delta V_{cath}). \quad (14)$$

$E_{e,iz}$ was calibrated by comparing the measured ionization threshold of various stable species such as nitrogen, hydrogen, ammonia, and methane, with their literature values (for nitrogen, see Table II). For both instruments, PM and MBMS, a shift ΔV_{cath} of -2 V was obtained and is taken into account in the following.

In contrast to unreactive gas particles, radical particles may get lost by contact with surfaces due to their reactivity. Therefore, it is crucial for a quantitative radical detection system that the particle beam from the plasma has no contact with chamber wall elements on the way to the ionizer. This is ensured in the case of the PM and MBMS (see Sec. II) where both electron-impact ionizers are in line of sight to the plasma volume.

B. Identification of atomic nitrogen

Fig. 3 shows for the PM the signal variation on mass channel 14 amu/e as function of $E_{e,iz}$ from 12 to 33 eV. To measure the thresholds for relevant conditions, the plasma off phase was not measured for cold N_2 gas but in the after-glow of a pulsed plasma. The signals shown are the steady state values at the end of the plasma on or plasma off phase, respectively. Each data point was acquired by summarizing many pulses for a fixed value of $E_{e,iz}$ with the MCS card. The plasma parameters for the discharge in pure N_2 shown in Fig. 3 are $p = 3$ Pa, a rf power of $P = 300$ W, $t_{on} = 10$ ms,

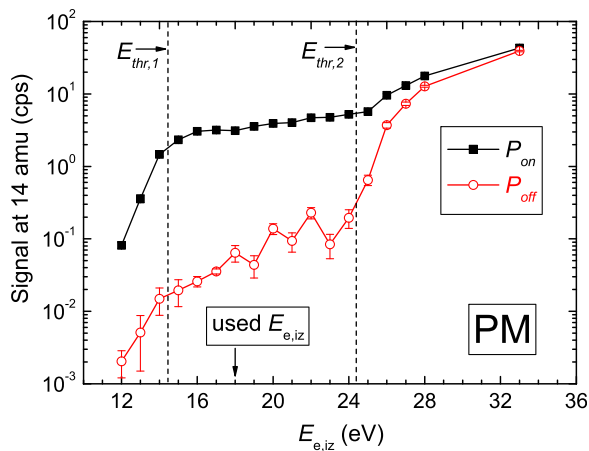


FIG. 3. Ionization threshold mass spectrometry of N^+ on mass channel 14 amu/e during plasma-on (P_{on}) and plasma-off (P_{off}) state in a N_2 discharge at a pressure of 3 Pa and a rf power of 300 W (pulsed mode: 10 ms P_{on} and 10 ms P_{off}) as function of the electron energy $E_{e,iz}$ of the ionizer measured with the PM. The threshold energies $E_{thr,1} = 14.5$ eV and $E_{thr,2} = 24.3$ eV of the direct ionization of N and dissociative ionization of N_2 from Table II are shown.

$t_{off} = 10$ ms, and $t_{dwell} = 1$ ms. With such a variation of $E_{e,iz}$, it is possible to distinguish the N^+ ions originating from atomic N from N^+ produced from molecular N_2 .

In Fig. 3, the PM signals for P_{on} and P_{off} are clearly different in the energy range of $12 \leq E_{e,iz} \leq 25$ eV. In this energy range, the PM signal during P_{on} is about one order of magnitude higher than that during P_{off} . For $E_{e,iz} > 25$ eV, the PM signals of P_{on} and P_{off} approach each other. Both PM signals are characterized by edges where the slope changes significantly. In Fig. 3, these edges are located at around 14 and 25 eV.

The PM signal in the electron energy region of $12 \leq E_{e,iz} \leq 25$ eV during P_{on} is assigned to atomic nitrogen from the plasma since only during P_{on} an explicit PM signal is measured. The PM signal for $E_{e,iz} > 25$ eV originates predominantly from molecular nitrogen which is abundant in both phases. Furthermore, the measured edges coincide within the experimental uncertainty with the threshold energies for direct ($E_{thr,1}(N \rightarrow N^+) = 14.5$ eV, Eq. (12)) and dissociative ionization ($E_{thr,2}(N_2 \rightarrow N^+) = 24.3$ eV, Eq. (13)).

A significant decrease of the PM signal with decreasing energy occurs in the range of $12 \leq E_{e,iz} \leq 15$ eV. One would expect that below $E_{thr,1}(N \rightarrow N^+) = 14.5$ eV, no significant PM signal would be detected. But the lowest electron energy where still a signal is measured is $E_{e,iz} = 12$ eV. This should be due to the fact that N^+ is not only produced by direct ionization of ground state $N(^4S)$, but also by direct ionization of the metastable states $N(^2D)$ and $N(^2P)$ which have ionization energies of 12.1 and 10.7 eV, respectively (Table II). The $N(^2D)$ threshold of $E_{thr}(N(^2D) \rightarrow N^+) = 12.1$ eV agrees with the observed value of $E_{e,iz} = 12$ eV. Therefore, we attribute the PM signal in the range of $12 \leq E_{e,iz} \leq 15$ eV to the metastable state $N(^2D)$.

For the measurement of the decay of atomic nitrogen with time in pulsed plasmas, a fixed electron energy $E_{e,iz}$ is used. With knowledge of Fig. 3 for the mass channel 14 amu/e, a $E_{e,iz}$ of 18 eV is selected for the measurements with the PM (see Sec. V).

In Fig. 4, equivalent measurements with the MBMS for the same plasma conditions are shown. Qualitatively, the behavior of the MBMS measurements is the same as in the case of the PM. A quantitative difference between them is

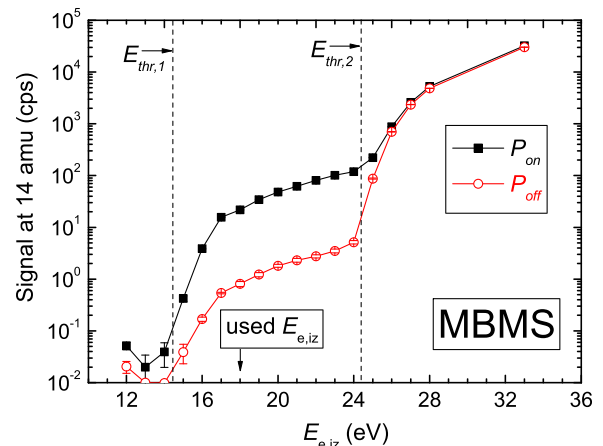


FIG. 4. Same as in Fig. 3 measured with the MBMS.

that in the MBMS measurement the energy of the edge between $12 \leq E_{e,iz} \leq 18$ eV in Fig. 4 is at (16 ± 1) eV, whereas for the PM measurement it is at (14 ± 1) eV. It is assumed that this lower edge of the PM measurement is due to $N(^2D)$. Therefore, it is concluded that at the plasma chamber side walls where the MBMS is located, the density of $N(^2D)$ is negligible. For the measurement of the relative radical density in pulsed plasmas (see Sec. V), a fixed electron energy of $E_{e,iz} = 18$ eV is used for the MBMS.

In Figs. 3 and 4, it can be seen that although there is a substantial difference between the P_{on} and P_{off} signals also in the P_{off} state, the signal during P_{off} is significant. However, even without plasma for pure N_2 gas in the chamber signals at 14 amu/e and $E_{e,iz} = 12$ eV are detected (average signal rate of 0.1 counts/s for the PM and 0.01 counts/s for the MBMS in steady state). These signals are attributed to dissociation of N_2 at the hot filament in the ion source of the mass spectrometers. The N_2 originates from the isotropic background gas in the mass spectrometer chambers. Such a dissociation of the parent molecule was also observed by Kae-Nune *et al.*³⁸ in ITMS measurements of atomic hydrogen.

So far, it was assumed for the ITMS technique that molecular nitrogen only occurs in the ground state. However, during plasma operation N_2 can also occur in vibrationally excited levels $N_2(vib)$ or as metastable $N_2(A)$ which denotes the $A^3\Sigma_u^+$ state of N_2 . In the following, the influence of vibrationally excited and metastable states which have lower threshold energy for N^+ production than ground state N_2 , is discussed. For the chosen electron energy of $E_{e,iz} = 18$ eV, excited N_2 molecules can be ionized if their potential energy is at least $24.3 \text{ eV} - 18 \text{ eV} = 6.3 \text{ eV}$ above the ground state of $N_2(X)$. An energy of 6.3 eV above the ground state corresponds to a vibrational level of about $v = 26$. The vibrational population can be estimated with a typical vibrational temperature of $T_{vib} = 11\,000 \text{ K}$ (see Ref. 39) to $N_2(vib)/N_2(X) \propto \exp(-6.3 \text{ eV}/1 \text{ eV}) = 0.002$. For a vibrational level higher than 6.3 eV ($v > 26$), the relative density is even lower than 0.002. For the cross section for the dissociative ionization of the vibrational levels ($v > 26$), we estimate that $\sigma_{N_2(vib) \rightarrow N^+}$ is of the order of $\sigma_{N \rightarrow N^+}$. Using Eq. (11), we summarize that the contribution of $N_2(vib)$ to the N^+ signal can be neglected for our conditions. The metastable state $N_2(A)$ has a density ratio $N_2(A)/N_2(X)$ in the order of $N/N_2(X)$ as shown by a rate equation model.¹⁶ The excitation energy of $N_2(A)$ is 6.3 eV. However, right at the threshold the cross section $\sigma_{N_2(A) \rightarrow N^+}(E_{e,iz} = 18 \text{ eV})$ goes to 0 and, hence, the influence of $N_2(A)$ on the N^+ signal can also be neglected.

The linearity of the intensity scales of the SEMs of the mass spectrometers is a further prerequisite for the measurement of the decay time. The linearity was checked by two methods. First, the isotopic ratio of neon was measured and compared to the theoretical isotopic ratio. A description of the procedure can be found in Ref. 13. Both measured and theoretical ratios agree within the experimental uncertainty. Second, the decay of the Ar signal is measured with both the PM and the MBMS after stopping the gas supply of Ar into the plasma chamber. The experiment was carried out for two different initial Ar pressures. Both measuring devices show

that the signal decay is exponential as function of the time over an intensity range of more than 4 orders of magnitude. Likewise, both measuring devices yield the same decay time. Based on these experimental results, we conclude that both instruments the PM as well as the MBMS have a linear intensity scale in the range of interest here.

V. RESULTS

Measurements were carried out in pure N_2 plasmas for pressures of 3.0, 5.0, 7.5, and 10.0 Pa. The plasma parameters n_e and T_e determined with the Langmuir probe and $T_{rot}^{N_2}$ determined by OES are shown in Table III together with the plasma conditions. The rf power was adjusted such that the variation of the electron density with increasing pressure is minimized. n_e was kept at $n_e = (3.7 \pm 0.1) \times 10^{16} \text{ m}^{-3}$. As expected, T_e decreases with increasing pressure from 2.7 to 2.0 eV. $T_{rot}^{N_2}$ increases with increasing pressure from 560 K at 3.0 Pa to 660 K at 10.0 Pa and thus varies by 100 K. The mean value of $T_{rot}^{N_2}$ is 610 K which will be used as gas temperature T_g in the following for all pressures.

The internal plasma parameters n_e , T_e , and $T_{rot}^{N_2}$ listed in Table III were measured in steady-state plasmas without pulsing. On a time scale of $\leq 100 \mu\text{s}$ after plasma ignition, the electron temperature and electron density reach steady state.^{40–42} Therefore, it is assumed that the measured T_e and n_e of the steady state plasmas are also valid for the pulsed plasmas for $t > 100 \mu\text{s}$. The plasma electrons take a key position in the heating mechanism of the gas species^{13,23} (e.g., heating by electron-induced dissociation of the stable molecular gas species) resulting in a certain gas temperature. It is assumed that once T_e and n_e are in steady state, also the rotational temperature is in steady state.

Nitrogen radicals are produced by electron-induced dissociation of N_2 and are lost by recombination at the wall. In this work, the temporal afterglow of the P_{off} phase for times larger than $100 \mu\text{s}$ is considered. Within a time scale of less than $10 \mu\text{s}$, the electron temperature decreases to less than 1 eV (see Refs. 40 and 41) so that plasma electrons are no longer able to dissociate or ionize gas species. Therefore, the afterglow measurements of the present work show only the loss process of the radicals.

As discussed in Sec. IV, the mass spectrometers PM and MBMS operate on the mass channel 14 amu/e using an electron energy of $E_{e,iz} = 18$ eV to measure the relative N atom density in neutral gas mode during the pulsed N_2 plasma.

TABLE III. Used plasma conditions (p —total pressure, P_{rf} —rf power, t_{on} —duration of plasma-on phase, t_{off} —duration of plasma-off phase) and measurement results (n_e —electron density, T_e —electron temperature, $T_{rot}^{N_2}$ —rotational temperature of N_2) of the considered N_2 plasma. n_e , T_e were measured with the Langmuir probe and $T_{rot}^{N_2}$ with OES in steady-state plasmas.

p (Pa)	P_{rf} (W)	t_{on} (ms)	t_{off} (ms)	n_e (10^{16} m^{-3})	T_e (eV)	$T_{rot}^{N_2}$ (K)
3.0	300	2	20	3.6	2.7	560
5.0	250	3	30	3.8	2.3	590
7.5	220	5	50	3.7	2.1	620
10.0	205	10	100	3.6	2.0	660

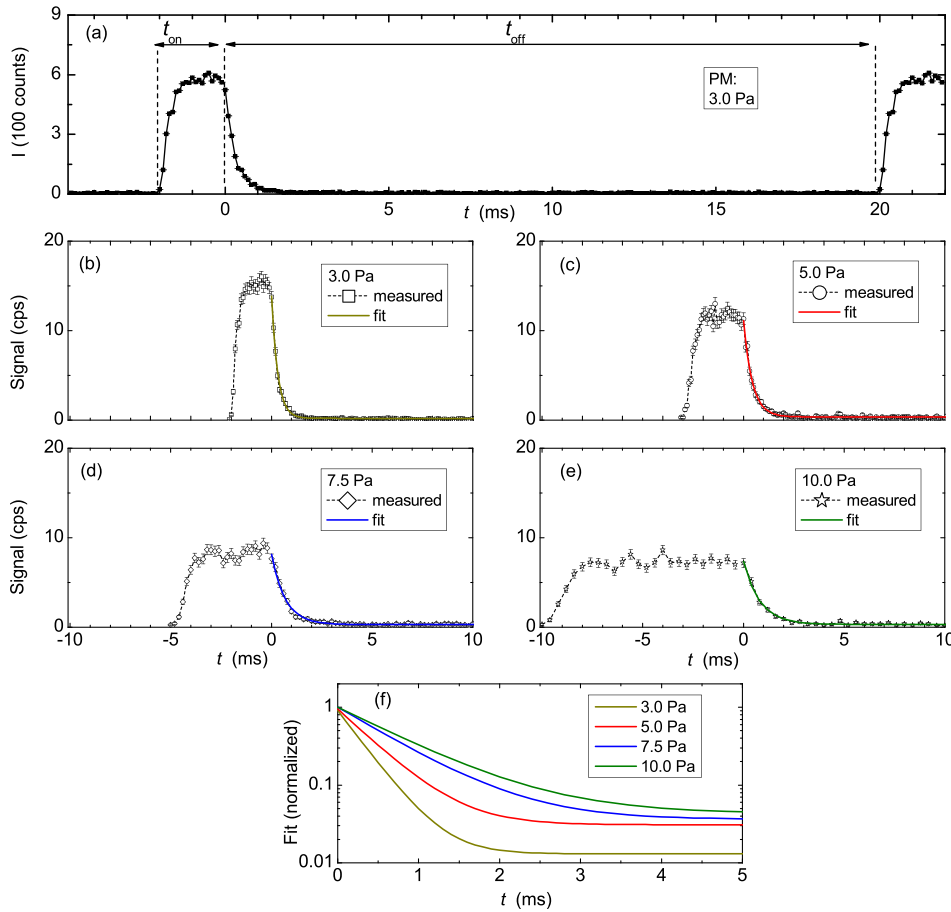


FIG. 5. Signal at mass channel 14 amu/e and an electron energy of 18 eV measured with the PM in a pulsed N₂ plasma for different pressures as function of time t . (a) Shows the signal for a complete pulse cycle consisting of the power-on phase with time t_{on} and power-off phase with time t_{off} . Measurements and corresponding fit curves are shown for the pressures 3.0 Pa (b), 5.0 Pa (c), 7.5 Pa (d), and 10.0 Pa (e). The x-axis is chosen such that at $t=0$ the power-off phase starts. In (f), normalized fit curves are shown for comparison.

The duration times t_{on} and t_{off} of the P_{on} and P_{off} phases for different pressures were chosen such that the decay process can be measured optimally. The duty cycle $t_{on}/(t_{on} + t_{off})$ is constant for all studied pressures. The used t_{on} and t_{off} are included in Table III. The signals of the PM for the different investigated pressures are shown in Fig. 5 as a function of time t . In Fig. 5(a), the signal (absolute number of counts) is shown for a full pulse at a pressure of 3 Pa. For this measurement, 3.8×10^5 full cycles were accumulated. With a dwell time of 10^{-4} s and a number of channels of 220, this corresponds to a total measurement time of more than 2 h. The P_{on} phase is characterized by a fast signal increase within the first 0.8 ms. Then, the signal saturates and remains constant for the remaining P_{on} time. The absolute number of counts is about 600 resulting in good counting statistics (counting error $\sim 4\%$). In the P_{off} phase, the signal falls off rapidly within the first 4 ms. For larger times t in the P_{off} phase, the signal exhibits a small background. For all studied pressures, the background signal of the PM is within the experimental uncertainty constant at about 0.2 cps. The x-axis (time t) is chosen such that at $t=0$ the power-off phase starts. In Figs. 5(b)–5(e), the signals for 3.0, 5.0, 7.5, and 10.0 Pa are shown together with the fit curves (see below). The signals of Figs. 5(b)–5(e) are converted to counts per second. The x and y axes in Figs. 5(b)–5(e) are for all plots the same. Therefore, the signals can be compared with each other. For the different considered pressures, different t_{on} and t_{off} values (Table III) were chosen. Therefore, the measurement at 3 Pa starts at $t=-2$ ms and the measurement at $p=10$ Pa at

$t=-10$ ms. The steady-state signal of the P_{on} phase decreases with increasing pressure.

In the P_{off} phase, the signal decreases exponentially. The following exponential function is used to fit the data:

$$y = Ce^{(-t/t_{wN})} + y_0. \quad (15)$$

C and y_0 are fitting constants and t_{wN} is the decay time. y_0 accounts for the signal background for large t . For better comparison, the normalized ($y(t=0)=1$) fit curves are shown together in one plot in Fig. 5(f). It can be clearly seen

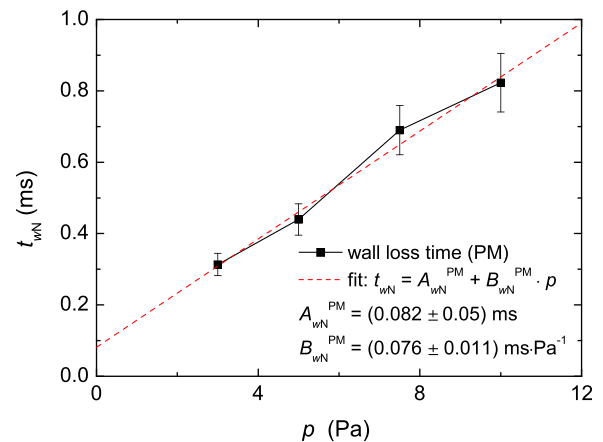


FIG. 6. Wall loss time t_{wN} of atomic nitrogen from afterglow measurements in a N₂ plasma as function of the pressure p measured with the PM (black squares). A fit of t_{wN} as a function of p is shown as dashed curve.

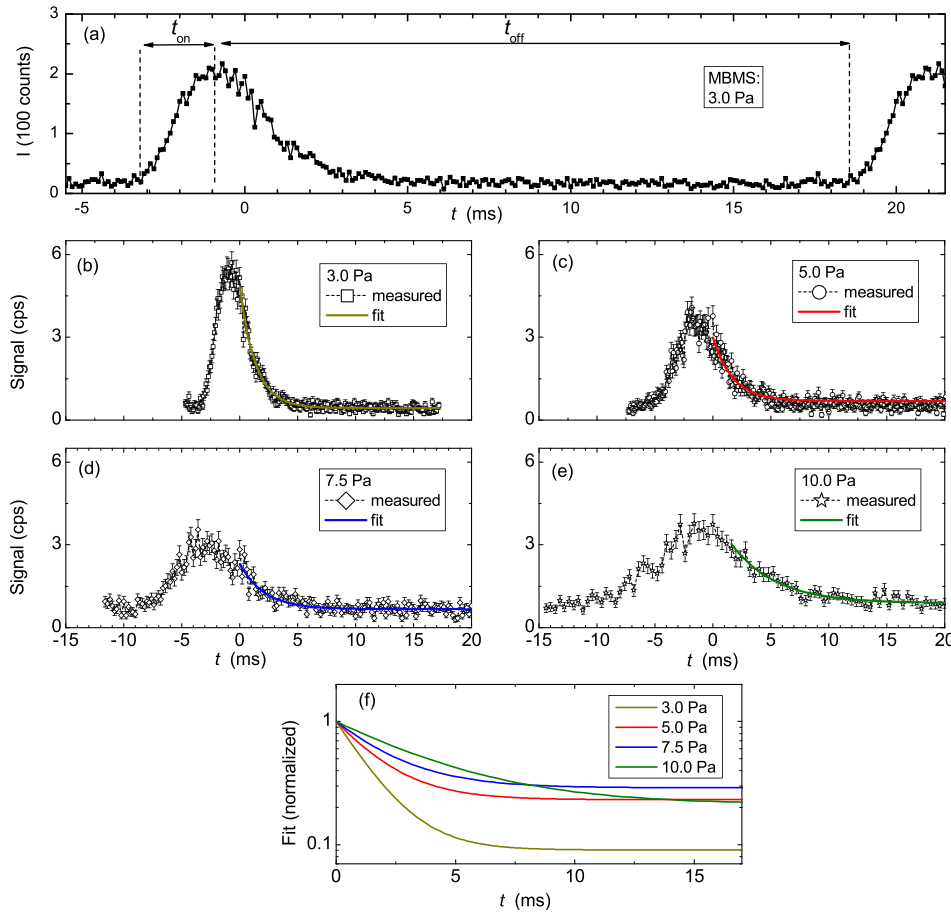


FIG. 7. Signal at mass channel 14 amu/e and an electron energy of 18 eV measured with the MBMS in a pulsed N_2 plasma for different pressures as function of time t . (a) Shows the signal for a complete pulse cycle consisting of the power-on phase with time t_{on} and power-off phase with time t_{off} . Measurements and corresponding fit curves are shown for the pressures 3.0 Pa (b), 5.0 Pa (c), 7.5 Pa (d), and 10.0 Pa (e). The x-axis is chosen such that at $t=0$ the power-off phase starts. In (f), normalized fit curves are shown for comparison.

that with increasing pressure the decay time increases. The such determined decay times are plotted in Fig. 6 as function of p . t_{wN} increases linearly from 0.31 to 0.82 ms as p increases from 3.0 to 10.0 Pa. The t_{wN} data as function of p are fitted using a linear fit with the fitting constants A_{wN} and B_{wN} which are the intersection with the y-axis and the slope, respectively. The values are $A_{wN}^{PM} = 8.2 \times 10^{-5}$ s and $B_{wN}^{PM} = 7.6 \times 10^{-5}$ s Pa $^{-1}$. It has to be mentioned that in Fig. 5(f) the background level cannot be compared with each other for different pressures because these are normalized curves with different background-to-maximum ratios.

The data measured by MBMS at the sidewall of the plasma chamber are shown in Fig. 7. These data are measured simultaneously with the PM data shown in Fig. 5. Qualitatively, the results are similar to the PM measurements of Fig. 5. However, the signal peak is much broader. The signal during P_{on} just reaches a maximum. The decay of the MBMS signals in the afterglow is also fitted according to Eq. (15). Due to the fact that the signals as function of t do neither show a clear saturation nor a distinct start of the decay at $y(t=0)$, the fit was applied for slight higher values of $t > 0$ ($0 < t < 0.1$ ms for 3.0 to 7.5 Pa, 1.6 ms for 10.0 Pa measurement) where a decay can be observed clearly (Figs. 7(b)–7(e)). For the same pressure, the decay times measured with the MBMS are longer than these of the PM. Similar to the PM measurements, they increase with increasing pressure. These decay times are plotted in Fig. 8 as function of p . t_{wN} increases linearly from 1.4 to 3.8 ms as p increases from

3.0 to 10.0 Pa. A linear fit for t_{wN} as function of p yields $A_{wN}^{MBMS} = 5.5 \times 10^{-4}$ s and $B_{wN}^{MBMS} = 2.7 \times 10^{-4}$ s Pa $^{-1}$. The most important difference between the MBMS and the PM measurement is that t_{wN} measured with the MBMS is considerably larger than that of the PM measurement. Furthermore, the slopes are different. The slope ratio is $B_{wN}^{MBMS}/B_{wN}^{PM} = 3.6 \pm 0.9$. To clarify this difference, a model of the wall loss time will be discussed in the following section.

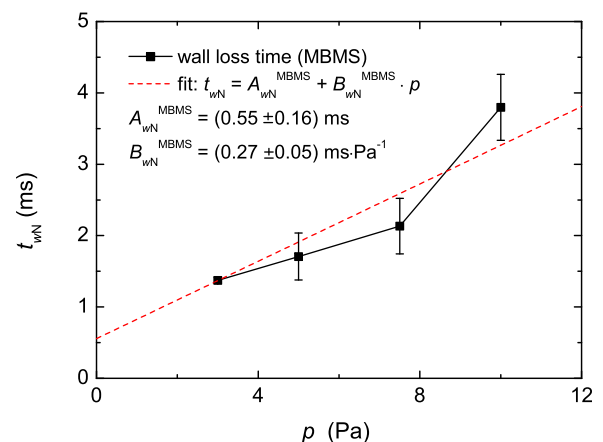


FIG. 8. Wall loss time t_{wN} of atomic nitrogen from afterglow measurements in a N_2 plasma as function of the pressure p measured with the MBMS (black squares). A fit of t_{wN} as a function of p is drawn as dashed curve.

VI. DISCUSSION

A. Theoretical description of the wall loss time

In N_2 plasmas, the N atoms are produced almost exclusively from the electron-induced dissociation of N_2 with the corresponding rate coefficient K_{diss} and are lost to the wall. The wall loss is determined by diffusion and a surface loss part where N atoms recombine to form N_2 . Other loss processes such as three-body recombination in the plasma volume or pumping can be neglected for the present conditions.^{3,4} The wall loss time t_{wN} , which is the inverse of the wall loss rate coefficient, is the mean time for a nitrogen atom to get lost at the plasma surrounding wall. In a zero dimensional ansatz, the N atom density is given by the continuity equation:

$$\frac{\partial n_N}{\partial t} = 2n_{N_2} \times n_e \times K_{diss}(T_e) - \frac{n_N}{t_{wN}}. \quad (16)$$

In the plasma afterglow N atoms are no longer generated from the electron-induced dissociation of N_2 since the energy of the electrons drops sharply within a few μs after switching off the rf power.^{40,41} The loss process, though, takes place in the millisecond range. Therefore, in the afterglow, Eq. (16) simplifies to

$$\frac{\partial n_N}{\partial t} = -\frac{n_N}{t_{wN}}. \quad (17)$$

If t_{wN} is constant as function of t , the solution of the differential Eq. (17) is an exponential decay of the N density

$$n_N = n_{N,0} \times e^{-t/t_{wN}} \quad (18)$$

with $n_{N,0}$ being the N density at $t=0$, i.e., the N density at the time when plasma is switched off. The observed decay of the measured atomic nitrogen signals in the P_{off} phase is exponential (see Sec. V). Based on this, we assign the experimentally obtained decay time of the afterglow measurements to the wall loss time. In general, t_{wN} can be described by a diffusive part t_{DN} and a surface loss part t_{sN} :^{43,44}

$$t_{wN} = t_{sN} + t_{DN}. \quad (19)$$

The surface loss time is given by^{15,43}

$$t_{sN} = \frac{V}{A} \frac{2(1 - \beta_N)}{\beta_N} \frac{1}{v_N} \quad (20)$$

(V —plasma volume, A —surface area where N can be lost, β_N —surface loss probability for N, $v_N = \sqrt{8k_B T_N / \pi M_N}$ —mean velocity of N, M_N —mass of N, T_N —temperature of N). The diffusion time of atomic nitrogen is given by^{15,43}

$$t_{DN} = \frac{\Lambda^2}{D_N} = \frac{\Lambda^2 \times p}{\tilde{D}_N} \quad (21)$$

with Λ being the diffusion length, D_N the diffusion constant, and \tilde{D}_N the pressure-independent diffusion constant. Since t_{wN} is a linear function of p , it is more convenient to rewrite Eq. (19) as a function of p

$$t_{wN} = A_{wN} + B_{wN} \times p \quad (22)$$

with

$$A_{wN} = t_{sN} \quad (23)$$

and

$$B_{wN} = \frac{\Lambda^2}{\tilde{D}_N}. \quad (24)$$

The intersection A_{wN} of t_{wN} with the y-axis and the slope B_{wN} were determined experimentally in Sec. V from the measurements of t_{wN} for different pressures. According to Eqs. (23) and (24), A_{wN} and B_{wN} are identified with the surface loss time and the diffusive part, respectively. As can be seen in Figs. 6 and 8, A_{wN} has a rather low contribution on the measured t_{wN} . For example, for the t_{wN} measurement with the PM presented in Fig. 6, A_{wN} contributes at the lowest considered pressure of 3 Pa with 26% to t_{wN} . For higher pressures, the contribution is even lower. Therefore, for our case, t_{wN} is dominated by diffusion, i.e., $t_{wN} \approx t_{DN}$.

For the diffusion constant, several models^{16,45} exist depending on the intermolecular potential for the collision of N with N_2 . Furthermore, the diffusion constant is a function of the particle temperature. The temperature of the N atom is, however, *a priori* unknown. Here, we assume that the N temperature is equal to the background gas temperature for the considered plasma conditions.⁸

With the chosen zero-dimensional ansatz, t_{wN} is a function of the geometry of the plasma chamber. In this respect, the volume to surface area ratio V/A is an important parameter for the description of t_{sN} (see Eq. (20)) and the diffusion length Λ for t_{DN} (see Eq. (21)). In our experimental setup, the geometry of the plasma chamber does not have a simple cylindrical geometry and the plasma-surrounding walls consist of different materials (Fig. 1) which have different β_N (see Eq. (20)). Therefore, a simple cylindrical geometry cannot be applied and further assumptions have to be made. Furthermore, the positions of the mass spectrometers are important. The PM measures the N density at the radial center of the plasma volume ($r=0$ mm and $l=30$ mm), whereas the MBMS measures at the radial side walls ($r=200$ mm and $l=0$ mm). Therefore, the relevant geometry has to be discussed individually for both setups.

The following considerations shall illustrate that the different wall loss times measured with the MBMS and PM can be attributed to the different positions of the mass spectrometers in the plasma chamber which leads to a different effective geometry. In doing this, the ratio $B_{wN}^{MBMS}/B_{wN}^{PM}$ of the slopes determined from the linear fits in Figs. 6 and 8 will be estimated based on a model for t_{wN} . According to Eq. (24), the ratio of the slopes is independent of the diffusion constant. $B_{wN}^{MBMS}/B_{wN}^{PM}$ is, therefore, equal to the ratio of the square of the diffusion lengths $(\Lambda^{MBMS}/\Lambda^{PM})^2$. For cylindrical geometry, Λ is given by⁴³

$$\frac{1}{\Lambda^2} = \left(\frac{\pi}{l}\right)^2 + \left(\frac{2.405}{r}\right)^2. \quad (25)$$

Now, the effective Λ has to be discussed for both PM and MBMS. For the PM, a cylinder without radial side wall at $r = r_{el}$ between the upper electrode and the quartz window is considered as the relevant volume. Because there is no radial side wall at r_{el} and due to an aspect ratio $l_{el}/r_{el} \lesssim 1$, only axial losses to the upper stainless steel electrode or lower quartz dome are taken into account. This is equivalent to $r \rightarrow \infty$ (see Ref. 15) such that the second term in Eq. (25) vanishes. In our experiment, the plasma interacts with two chamber wall materials: stainless steel (electrode) and quartz (dielectric window). Quartz has a significantly lower β_N than stainless steel (see Ref. 46). Therefore, it is assumed that atomic nitrogen is lost only at the stainless steel electrode.¹⁵ For the PM, the diffusion length is obtained by solving the diffusion equation for a 1-dimensional case where the radical is lost on the one and reflected on the other electrode surface. The result is $\Lambda^{PM} = l_{el}/\sqrt{3} = 35$ mm (for details, see Ref. 16). For the MBMS, the geometry is rather complex. The MBMS measures at the radial side walls of the chamber. As simplest approach, a cylinder with $l = l_{ch} = 360$ mm and $r = 200$ mm which is the distance between plasma center and MBMS entrance orifice is assumed. Since $l_{ch} > r = 200$ mm, Eq. (25) can be simplified to $\Lambda^{MBMS} \approx r/2.405 = 83$ mm. Under these assumptions, the ratio of the slopes is:

$$B_{wN}^{MBMS}/B_{wN}^{PM} = (\Lambda^{MBMS}/\Lambda^{PM})^2 \approx \left(\frac{r}{2.405} \times \frac{\sqrt{3}}{l_{el}} \right)^2 = 5.8. \quad (26)$$

For comparison, the experimentally obtained slope ratio of Sec. V is $B_{wN}^{MBMS}/B_{wN}^{PM} = 3.6 \pm 0.9$. It has to be noted that $\Lambda^{MBMS} = 83$ mm is only a very rough upper estimate. Considering Eq. (25) and noting that l is finite and a significant loss of radicals occurs at the steel electrode, Λ^{MBMS} should be substantially smaller than 83 mm resulting in a lower slope ratio. Despite the large inherent uncertainties, Eq. (26) yields a rough estimate of the experimentally obtained slope ratio. Summarizing, the difference of wall loss times measured with MBMS and PM is attributed to the different diffusion lengths.

As final result, we will derive the surface loss probability β_N of atomic nitrogen on stainless steel from the wall loss time data of the PM. For this, the intersection A_{wN} of t_{wN} with the y-axis of Fig. 6 is analyzed applying Eqs. (20) and (23). For the analysis, the volume to surface ratio and the radical temperature have to be known. The volume of the assumed cylinder is $V = \pi r_{el}^2 l_{el}$. As mentioned above, the atomic nitrogen radical is lost only at the area of the upper electrode, i.e., $A = \pi r_{el}^2$ (see Ref. 15). Therefore, the volume to surface ratio is $V/A = l_{el}$. As also discussed above, the radical temperature is assumed to be equivalent to the gas temperature ($T_N = T_g$). With the experimentally obtained value of $A_{wN}^{PM} = (8.2 \pm 5) \times 10^{-5}$ s, Eqs. (20) and (23), and the assumptions for V/A and T_N a β_N of 1.2 ± 0.3 is derived. A surface loss probability of higher than 1 is not reasonable. Therefore, it is concluded that the surface loss probability of atomic nitrogen on stainless steel lies in the range of 0.9 to 1.0 for the conditions of our experiment.

Due to the larger scatter of the MBMS data resulting in a much larger uncertainty of A_{wN}^{MBMS} , we cannot derive a β_N from these data. Nevertheless, we can infer a large β_N from the MBMS data because as mentioned in Sec. II B no significant N signal is detected when the stainless steel shutter blocks the beam inside the MBMS chamber. For low β_N , N should survive many wall collisions and reach the ionizer. This is not the case. Therefore, we conclude that β_N measured with the MBMS is expected to be comparably large as for the PM measurements.

B. Comparison with literature

Takashima *et al.*⁵ determined t_{wN} in the afterglow of a pulsed capacitively coupled N₂ plasma with VUVAS in the pressure range from 1.3 to 27 Pa. The measured t_{wN} corresponds to the wall loss time. t_{wN} increases linearly from 10 to 20 ms as p increases from 1.3 to 13 Pa. Hence, t_{wN} is proportional to the pressure which is in agreement with the results of the present work. Takashima *et al.* used the same model for the description of t_{wN} as in the present work (see Sec. IV). They determined a β_N of 0.03 for N on stainless steel for an atomic nitrogen temperature of 400 K, which is a factor of 30 smaller than the one determined here.

Kang *et al.*⁶ investigated experimentally the N atom density in a pulsed inductively coupled N₂ plasma as a function of time in the afterglow with TALIF. The absolute N atom density in the afterglow was shown for 2.7 and 27 Pa and exhibits a simple exponential decrease with time. The decay times were determined for pressures between 2.7 and 1000 Pa. The lowest decay time was measured for a pressure of 2.7 Pa and was $t_{wN} = 3.3$ ms. t_{wN} is almost constant up to a pressure of about 40 Pa. For higher pressures $p > 40$ Pa, t_{wN} increased with increasing pressure. Kang *et al.* used also the same theory for the description of t_{wN} as the present work (see Sec. VI). They took the measured N₂ rotational temperature of 400 K as gas temperature and as the N temperature, too. A β_N of 0.02 gave a good agreement between the calculated and the measured t_{wN} as a function of p . 2/3 of the plasma chamber wall of Kang *et al.* consisted of stainless steel and 1/3 of glass. For calculation of β_N from t_{wN} , the whole wall loss area was considered. Therefore, the obtained β_N is a mean value for the two different wall materials. The specified β_N in Kang *et al.* is an average over values for various surfaces.

The similarities between Kang *et al.*, Takashima *et al.*, and the present study are that both observed in the afterglow of a pulsed plasma a simple exponential decrease of the N atom density with time and the measured t_{wN} is well described by a diffusion model (see Sec. VI). In spite of similarities in discharge geometries, discharge volumes, pressure range, and similar power densities, the measured wall loss times of Refs. 5 and 6 are at least one order of magnitude higher than the values of the present work. Because both Refs. 5 and 6 apply the same model as in the present work, this difference in t_{wN} leads also to more than one order of magnitude difference in β_N . We can only speculate about the reason for this. One possibility could be a different surface temperature. Therefore, we consider the work of Gaboriau *et al.*¹⁰

Gaboriau *et al.*¹⁰ determined β_N of N on iron in a glass reactor at 40–400 Pa in the P_{off} phase. They determined β_N with a fiber optic catalytic probe (see also Ref. 11). They determined β_N for various pressures. In the range between $130 < p < 400$ Pa β_N is independent of pressure. In the range between $40 < p < 130$ Pa, β_N increases with decreasing p . For a surface temperature of 400 K, β_N increases from 0.06 (130 Pa) to 0.33 (40 Pa) but no interpretation of this increase was provided. Furthermore, they studied two different temperatures of the catalytic probe: 310 and 400 K. They observed for $130 < p < 400$ Pa an increase of β_N from 0.02 (310 K) to 0.06 (400 K) by a factor of 3 and thus showed that β_N depends sensitively on the temperature of the surface.

If we assume that the relevant surface temperature is equal to the measured gas temperature, we come to the following considerations: In the work of Takashima *et al.*⁵ and Kang *et al.*,⁶ the gas temperature was 400 K. In contrast, in our experiments, the measured gas temperature was 600 K. Accordingly, the surface temperature in our experiment is assumed to be 600 K, while it is only 400 K in the other two references.^{5,6} As shown by Gaboriau *et al.*, a higher surface temperature causes a higher β_N . Therefore, we suppose that the difference between Refs. 5 and 6 and the present work is due to the considerable different temperatures.

Another issue is the surface condition of the plasma chambers for the different studies. For the capacitively coupled plasma of Takashima *et al.*,⁵ the quartz window is most probably sputtered and the sputtered material is re-deposited as thin film on the stainless steel surface. For Kang *et al.*,⁶ we can only speculate that capacitive coupling was also present to some extent from his planar coil. At least in the beginning, we observed quartz sputtering in our setup using standard matching. To minimize sputtering, we have made substantial effort to suppress capacitive coupling of our ICP to avoid ions with high energies.^{13,47} In a former publication,¹³ we showed that in our inductively coupled plasma, the ion energies are of the order of 20 eV and, therefore, sputtering of quartz can be neglected. Furthermore, comparisons between the stainless steel electrode and an exchangeable electrode cover made of stainless steel result in the same surface loss probability of hydrogen in the case of hydrogen plasmas (see Ref. 8). Therefore, it is concluded that the stainless steel surface of our plasma chamber is not modified during plasma operation and that the plasma-surface interaction of the radicals occurs with clean stainless steel.

In this context, we want to add the following remark: Also for Pyrex different research groups obtained very different β_N values. As can be seen in Fig. 6 of Ref. 48, published values for β_N on Pyrex measured vary by up to two orders of magnitude. Therefore, in future studies, more attention has to be paid on critical parameters highlighted in this study such as surface condition (temperature, purity), vessel geometry, and radical temperature.

VII. SUMMARY

In the afterglow of a pulsed inductively coupled N₂ plasma, relative N atom densities were measured as a function of time by ITMS in order to determine the wall loss time

t_{wN} from the exponential decay curves. The procedure was performed with two mass spectrometers at different positions in the plasma chamber to study the dependence of t_{wN} on the positions in the plasma chamber. The first mass spectrometer (PM) was located in the radial center of the plasma chamber. The second mass spectrometer (MBMS) measured the radical density on the radial side walls of the plasma chamber.

The wall loss times were determined for pressures of 3.0, 5.0, 7.5, and 10 Pa. For these conditions also the internal plasma parameters electron density n_e and electron temperature T_e determined with a Langmuir probe and the rotational N₂ temperature $T_{\text{rot}}^{\text{N}_2}$ determined with optical emission spectroscopy were measured. For $T_{\text{rot}}^{\text{N}_2}$, a procedure was presented to evaluate the spectrum of the transition $v' = 0 \rightarrow v'' = 2$ of the second positive system ($C^3\Pi_u \rightarrow B^3\Pi_g$) of N₂. With this method, a gas temperature of 610 K was determined. It is assumed that the temperature of atomic nitrogen is equal to the gas temperature.

With the two mass spectrometers, it was observed that the wall loss times of atomic nitrogen increase with increasing pressure. The wall loss time measured in the radial center of the plasma chamber increases linearly from 0.31 ms for 3 Pa to 0.82 ms for 10 Pa. The wall loss time measured at the vessel wall is about 4 times larger than that of the PM. A model was applied to describe the measured t_{wN} . The main loss mechanism of atomic nitrogen for the considered pressure range is diffusion to the wall. The surface loss probability β_N of atomic nitrogen on stainless steel was derived from t_{wN} and was found to be about unity (0.9–1.0) for the present conditions. With the model, it was shown that the difference of wall loss times measured at the two positions can be attributed to the different diffusion lengths.

ACKNOWLEDGMENTS

We gratefully acknowledge help from T. Dürbeck for technical assistance.

¹S. Lee, S. Bang, S. Jeon, S. Kwon, W. Jeong, S. Kim, and H. Jeon, "Characteristics of hafnium-zirconium-oxide film treated by remote plasma nitridation," *J. Electrochem. Soc.* **155**, H516–H519 (2008).

²C. Hinkle and G. Lucovsky, "Remote plasma-assisted nitridation (RPN): applications to Zr and Hf silicate alloys and Al₂O₃," *Appl. Surf. Sci.* **216**, 124–132 (2003); in Proceedings of the Fourth International Symposium on the Control of Semiconductor Interfaces Karuizawa, Japan, October 21–25, 2002.

³E. G. Thorsteinsson and J. T. Gudmundsson, "A global (volume averaged) model of a nitrogen discharge: I. steady state," *Plasma Sources Sci. Technol.* **18**, 045001 (2009).

⁴H. Singh, J. W. Coburn, and D. B. Graves, "Recombination coefficients of O and N radicals on stainless steel," *J. Appl. Phys.* **88**, 3748–3755 (2000).

⁵S. Takashima, K. Takeda, S. Kato, M. Hiramatsu, and M. Hori, "Surface loss probability of nitrogen atom on stainless-steel in N₂ plasma afterglow," *Jpn. J. Appl. Phys., Part 1* **49**, 076101 (2010).

⁶N. Kang, F. Gaboriau, S.-G. Oh, and A. Ricard, "Modeling and experimental study of molecular nitrogen dissociation in an Ar-N₂ ICP discharge," *Plasma Sources Sci. Technol.* **20**, 045015 (2011).

⁷S. F. Adams and T. A. Miller, "Surface and volume loss of atomic nitrogen in a parallel plate rf discharge reactor," *Plasma Sources Sci. Technol.* **9**, 248 (2000).

⁸M. Sode, T. Schwarz-Selinger, W. Jacob, and H. Kersten, "Surface loss probability of atomic hydrogen for different electrode cover materials investigated in H₂-Ar low-pressure plasmas," *J. Appl. Phys.* **116**, 013302 (2014).

⁹H. Kersten, D. Rohde, J. Berndt, H. Deutsch, and R. Hippler, "Investigations on the energy influx at plasma processes by means of a

- simple thermal probe," *Thin Solid Films* **377–378**, 585–591 (2000); in International Conference on Metallurgical Coatings and Thin Films.
- ¹⁰F. Gaboriau, U. Cvelbar, M. Mozetič, A. Erradi, and B. Rouffet, "Comparison of TALIF and catalytic probes for the determination of nitrogen atom density in a nitrogen plasma afterglow," *J. Phys. D: Appl. Phys.* **42**, 055204 (2009).
 - ¹¹M. Mozetič, U. Cvelbar, A. Vesel, A. Ricard, D. Babic, and I. Poberaj, "A diagnostic method for real-time measurements of the density of nitrogen atoms in the postglow of an Ar–N₂ discharge using a catalytic probe," *J. Appl. Phys.* **97**, 103308 (2005).
 - ¹²J. Röpcke, P. B. Davies, N. Lang, A. Rousseau, and S. Welzel, "Applications of quantum cascade lasers in plasma diagnostics: a review," *J. Phys. D: Appl. Phys.* **45**, 423001 (2012).
 - ¹³M. Sode, T. Schwarz-Selinger, and W. Jacob, "Quantitative determination of mass-resolved ion densities in H₂-Ar inductively coupled radio frequency plasmas," *J. Appl. Phys.* **113**, 093304 (2013).
 - ¹⁴V. A. Kadetov, "Diagnostics and modeling of an inductively coupled radio frequency discharge in hydrogen," Ph.D. dissertation (Ruhr Universität Bochum, 2004).
 - ¹⁵M. Sode, T. Schwarz-Selinger, and W. Jacob, "Ion chemistry in H₂-Ar low temperature plasmas," *J. Appl. Phys.* **114**, 063302 (2013).
 - ¹⁶M. Sode, "Quantitative Beschreibung von Wasserstoff-Stickstoff-Argon-Mischplasmen," Ph.D. dissertation (Universität Kiel, 2013, in German).
 - ¹⁷M. Bauer, T. Schwarz-Selinger, H. Kang, and A. von Keudell, "Control of the plasma chemistry of a pulsed inductively coupled methane plasma," *Plasma Sources Sci. Technol.* **14**, 543–548 (2005).
 - ¹⁸M. Bauer, T. Schwarz-Selinger, W. Jacob, and A. v. Keudell, "Growth precursor for a-C:H film deposition in pulsed inductively coupled methane plasmas control of the plasma chemistry of a pulsed inductively coupled methane plasma," *J. Appl. Phys.* **98**, 073302 (2005).
 - ¹⁹W. Walcher, "Über eine Ionenquelle für massenspektroskopische Isotopentrennung," *Z. Physik.* **122**, 62–85 (1944).
 - ²⁰P. Scheubert, U. Fantz, P. Awakowicz, and H. Paulin, "Experimental and theoretical characterization of an inductively coupled plasma source," *J. Appl. Phys.* **90**, 587 (2001).
 - ²¹U. Fantz, "Emission spectroscopy of molecular low pressure plasmas," *Contrib. Plasma Phys.* **44**, 508–515 (2004).
 - ²²K. Behringer, "Diagnostics and modelling of ECRH microwave discharges," *Plasma Phys. Controlled Fusion* **33**, 997 (1991).
 - ²³V. M. Donnelly and M. V. Malyshev, "Diagnostics of inductively coupled chlorine plasmas: Measurements of the neutral gas temperature," *Appl. Phys. Lett.* **77**, 2467 (2000).
 - ²⁴G. P. Davis and R. A. Gottscho, "Measurement of spatially resolved gas-phase plasma temperatures by optical emission and laser-induced fluorescence spectroscopy," *J. Appl. Phys.* **54**, 3080–3086 (1983).
 - ²⁵T. Sakamoto, H. Matsuura, and H. Akatsuka, "Spectroscopic study on the vibrational populations of N₂ C³Π and B³Π states in a microwave nitrogen discharge," *J. Appl. Phys.* **101**, 023307 (2007).
 - ²⁶C. Biloiu, X. Sun, Z. Harvey, and E. Scime, "An alternative method for gas temperature determination in nitrogen plasmas: Fits of the bands of the first positive system (B³Π_g → A³Σ_u⁺)," *J. Appl. Phys.* **101**, 073303 (2007).
 - ²⁷S. Saloum, M. Naddaf, and B. Alkhaled, "Diagnostics of N₂-Ar plasma mixture excited in a 13.56 MHz hollow cathode discharge system: Application to remote plasma treatment of polyamide surface," *J. Phys. D: Appl. Phys.* **41**, 045205 (2008).
 - ²⁸B. Krames, "Räumliche Konzentrationsverteilungen von N₂-Triplett-Zuständen im elektrodennahen Plasma einer RF-Niederdruckentladung," Ph.D. dissertation (Technische Universität Chemnitz, 1999, in German).
 - ²⁹G. Herzberg, *Molekülspektren und Molekülstruktur. I.: Zweiatomige Moleküle* (Steinkopff, Dresden, 1939).
 - ³⁰H. Singh, J. W. Coburn, and D. B. Graves, "Appearance potential mass spectrometry: Discrimination of dissociative ionization products," *J. Vac. Sci. Technol. A* **18**, 299 (2000).
 - ³¹S. Matsuda, H. Shimozato, M. Yumoto, and T. Sakai, "Detection of nitrogen metastable molecules by using the threshold ionization mass spectrometry," *Electric. Eng. Jpn.* **147**, 17–24 (2004).
 - ³²Y.-K. Kim and J.-P. Desclaux, "Ionization of carbon, nitrogen, and oxygen by electron impact," *Phys. Rev. A* **66**, 012708 (2002).
 - ³³Y. Itikawa, "Cross sections for electron collisions with nitrogen molecules," *J. Phys. Chem. Ref. Data* **35**, 31–53 (2006).
 - ³⁴S. Agarwal, B. Hoex, M. C. M. van de Sanden, D. Maroudas, and E. S. Aydil, "Absolute densities of N and excited N₂ in a N₂ plasma," *Appl. Phys. Lett.* **83**, 4918–4920 (2003).
 - ³⁵B. Sourd, P. André, J. Aubreton, and M.-F. Elchinger, "Influence of the excited states of atomic nitrogen N(²D) and N(²P) on the transport properties of nitrogen. Part I: Atomic nitrogen properties," *Plasma Chem. Plasma Process.* **27**, 35–50 (2007).
 - ³⁶F. R. Gilmore, "Potential energy curves for N₂, NO, O₂ and corresponding ions," *J. Quant. Spectrosc. Radiative Transfer* **5**, 369–389 (1965).
 - ³⁷H. Singh, J. W. Coburn, and D. B. Graves, "Mass spectrometric detection of reactive neutral species: Beam-to-background ratio," *J. Vac. Sci. Technol. A* **17**, 2447–2455 (1999).
 - ³⁸P. Kae-Nune, J. Perrin, J. Guillon, and J. Jolly, "Mass spectrometry detection of radicals in SiH₄-CH₄-H₂ glow discharge plasmas," *Plasma Sources Sci. Technol.* **4**, 250–259 (1995).
 - ³⁹T. Kimura and H. Kasugai, "Experiments and global model of inductively coupled rf Ar/N₂ discharges," *J. Appl. Phys.* **108**, 033305 (2010).
 - ⁴⁰S. Ashida, M. R. Shim, and M. A. Lieberman, "Measurements of pulsed-power modulated argon plasmas in an inductively coupled plasma source," *J. Vac. Sci. Technol. A* **14**, 391–397 (1996).
 - ⁴¹M. A. Lieberman and S. Ashida, "Global models of pulse-power-modulated high-density, low-pressure discharges," *Plasma Sources Sci. Technol.* **5**, 145 (1996).
 - ⁴²M. Osiac, T. Schwarz-Selinger, D. O'Connell, B. Heil, Z. L. Petrovic, M. M. Turner, T. Gans, and U. Czarnetzki, "Plasma boundary sheath in the afterglow of a pulsed inductively coupled RF plasma," *Plasma Sources Sci. Technol.* **16**, 355–363 (2007).
 - ⁴³P. J. Chantry, "A simple formula for diffusion calculations involving wall reflection and low density," *J. Appl. Phys.* **62**, 1141–1148 (1987).
 - ⁴⁴M. A. Lieberman and A. J. Lichtenberg, *Principles of Plasma Discharges and Materials Processing* (John Wiley and Sons, Inc., Hoboken, NJ, 2005).
 - ⁴⁵G. N. Hays, C. J. Tracy, and H. J. Oskam, "Surface catalytic efficiency of a sputtered molybdenum layer on quartz and Pyrex for the recombination of nitrogen atoms," *J. Chem. Phys.* **60**, 2027–2034 (1974).
 - ⁴⁶K. Kutasi and J. Loureiro, "Role of the wall reactor material on the species density distributions in an N₂ O₂ post-discharge for plasma sterilization," *J. Phys. D* **40**, 5612 (2007).
 - ⁴⁷K. Polozhiy and T. Schwarz-Selinger, "Suppression of capacitive coupling in a pulsed inductively coupled RF discharge," (unpublished).
 - ⁴⁸L. Lefèvre, T. Belmonte, and H. Michel, "Modeling of nitrogen atom recombination on Pyrex: Influence of the vibrationally excited N₂ molecules on the loss probability of N," *J. Appl. Phys.* **87**, 7497–7507 (2000).